Check for updates

Advanced Functional Materials

ADVANCED FUNCTIONAL MATERIALS
www.afm-journal.de

RESEARCH ARTICLE

Synergistic Ion Exchange-Redox in an Ionic Covalent Organic Polymer: Enhanced Iodate Removal and Excellent Regenerability

Hai-Ruo Li[1] | Xuezhuo Jing[1] | Cheng-Peng Li[1] | Igor P. Gloriozov[2] | Yuri A. Ustynyuk[2] | Abdullah M. Al-Enizi[3] | Ayman Nafady[3] | Shengqian Ma[4]

[1]Academy of Interdisciplinary Studies on Intelligent Molecules, Tianjin Key Laboratory of Structure and Performance for Functional Molecules, College of Chemistry, Tianjin Normal University, Tianjin, China | [2]Department of Chemistry, M.V. Lomonosov Moscow State University, Moscow, Russia | [3]Department of Chemistry, College of Science, King Saud University, Riyadh, Saudi Arabia | [4]Department of Chemistry, University of North Texas, Denton, Texas, USA

Correspondence: Cheng-Peng Li (hxxylcp@tjnu.edu.cn) | Yuri A. Ustynyuk (yuriustynyuk@gmail.com) | Shengqian Ma (shengqian.ma@unt.edu)

Received: 13 December 2025 | **Revised:** 13 July 2026 | **Accepted:** 31 July 2026

Keywords: covalent organic polymer | electron transfer | iodate adsorption | ion exchange | redox chemistry

ABSTRACT

Radioactive iodate (IO_3^-), the dominant iodine species in nuclear wastewater, poses severe environmental threats. Here we present a dual-functional ionic covalent organic polymer (iCOP) that integrates cationic guanidinium sites with redox-active phenolic groups. This unique architecture enables a synergistic ion exchange–redox mechanism, where IO_3^- is rapidly captured through electrostatic attraction and hydrogen bonds, then reduced in situ to I_2/I_3^-. The adsorbent achieves a high IO_3^- capacity of 1093.7 mg g^{-1}, fast kinetics, and high removal efficiency in simulated nuclear-contaminated groundwaters (86.8% for Beishan; 95.7% for Hanford). Importantly, it is the first regenerable redox sorbent for radioactive IO_3^- remediation, retaining 74% capacity after three mild ascorbic acid treatments. Control studies with a series of iCOPs confirm that both functionalities are indispensable, with redox activity underpinning the extraordinary capacity. Density functional theory calculations further reveal a stepwise proton-coupled electron transfer pathway and cooperative binding-reduction behavior, establishing a design principle for porous materials that couple targeted capture with chemical conversion of hazardous radionuclides.

1 | Introduction

Nuclear energy offers a reliable, low-carbon alternative to fossil fuels, with global generation projected to reach record levels by 2025 [1]. However, the nuclear fission of uranium-235 produces considerable amounts of radioactive iodine isotopes, notably ^{129}I, and ^{131}I [2]. ^{129}I is regarded as a dominant dose contributor in the performance assessment of high-level waste repositories, owing to its extreme half-life (15.7 million years), high environmental mobility, and low affinity for common geological barriers [3]. Particularly, U.S. EPA maximum contaminant level (MCL) for ^{129}I in drinking water is only 0.0057 μg L^{-1}, which underscores its severe long-term risk. In contrast, ^{131}I, despite its shorter half-life, is highly radiotoxic, posing immediate threats such as thyroid dysfunction [4]. The Fukushima Daiichi nuclear disaster in 2011 highlighted these concerns, releasing large quantities of radioactive ^{131}I into the atmosphere [5]. Initially discharged as iodide (I^-), radioactive iodine oxidizes in oxygenated environments to form stable iodate (IO_3^-), the dominant species in nuclear wastewater and contaminated waters due to its high solubility and mobility

Hai-Ruo Li and Xuezhuo Jing contributed equally to this work.

All rights reserved, including rights for text and data mining and training of artificial intelligence technologies or similar technologies.
© 2026 Wiley-VCH GmbH

[6]. For instance, IO_3^- constitutes ~84% of total iodine in groundwater at the Hanford site [7], highlighting an urgent need for effective remediation. Despite significant research on capturing iodine vapor, iodide, and organoiodine compounds, targeted IO_3^- removal remains a significant challenge.

Adsorption is a promising approach for large-scale radioactive iodine capture, offering cost-effectiveness, and operational simplicity [8–13]. Conventional adsorbents like zeolites [14], gels [15], metal–organic frameworks (MOFs) [16, 17], and activated carbons often suffer from low active site density and slow kinetics [18]. Layered double hydroxides (LDHs) utilize anion exchange but exhibit poor selectivity and capacity for IO_3^- [19]. Redox-active materials incorporating silver or bismuth show stronger affinity [20, 21]. For instance, He et al. developed microflower-like Bi_2S_3 that facilitated redox conversion of IO_3^- through charge transfer with S^{2-}, achieving a high adsorption capacity of 875.6 mg g^{-1} [22]. However, concerns over metal leaching and chemical stability persist. Encapsulation of formic acids in LZU-111 to react with IO_3^- by He et al. achieve a record-high removal (2817.5 mg g^{-1}) via reduction pathway [23]. Recently, Wang et al. reported a nonporous ionic polymer (SCU-CPN-6) combined ion exchange and redox to achieve the 896 mg g^{-1} IO_3^- uptake, but its slow kinetics (~2 h for 99% removal) and lack of regenerability limit application [24]. These results highlight that integrating strong electrostatic attraction, efficient redox conversion, and effective confinement of the reduced iodine species within a metal-free polymeric network could overcome the existing limitations, enabling rapid, high-capacity IO_3^- removal without secondary pollution.

Covalent organic polymers (COPs) are ideal candidates for this integration, featuring tunable porosity, high stability, and metal-free compositions [24–27]. Crucially, covalent organic networks containing phenolic hydroxyl groups can utilize phenol–quinone redox chemistry [28, 29], which is thermodynamically favorable for reducing IO_3^- under acidic conditions. The redox potential of benzoquinone/hydroquinone (+0.64 V vs. NHE) is thermodynamically sufficient to reduce IO_3^- to I_2 or I^- under acidic conditions, given the higher standard potentials of IO_3^-/I_2 (+1.195 V vs. SHE) and IO_3^-/I^- (+1.085 V vs. SHE) [30, 31]. Furthermore, incorporating cationic functionalities into ionic COPs enhances electrostatic attraction toward anions like IO_3^-.

With these in mind, we synthesized a two-dimensional iCOP, DhaTG(Cl^-), featuring cationic guanidinium groups for ion exchange and redox-active phenolic groups. This dual-functional design enables a synergistic ion exchange–redox mechanism for heterogeneous solid-phase capture: guanidinium groups provide strong initial electrostatic binding of IO_3^-, followed by electron transfer from phenolic groups reducing IO_3^- to I_2/I_3^-, which are effectively encapsulated within the powder material (Figure 1). This localized confinement within the polymeric network yields a high IO_3^- adsorption capacity (1093.7 mg g^{-1}) with fast kinetics (99% removal within 1 h), thereby minimizing the long-term environmental risk of secondary release. To elucidate the synergistic effect, we systematically varied the ratio of redox and ion exchange sites in four structurally analogous polymers, confirming that both functionalities are essential for optimal performance. Furthermore, density functional theory (DFT) calculations support the proposed ion exchange and redox pathways. Notably, DhaTG(Cl^-) maintains exceptional efficiency in simulated Beishan and Hanford nuclear-contaminated groundwaters, even in the presence of high concentrations of competing anions.

2 | Results and Discussion

2.1 | Characterization of DhaTG(Cl^-)

DhaTG(Cl^-) was synthesized via a Schiff base condensation with 1,2,3-triaminoguanidine monohydrochloride (TG) and 2,5-dihydroxyterephthalaldehyde (Dha) (Figure 2a). Powder X-ray diffraction (PXRD) reveals a broad peak at around 5.2° and a diffuse feature near 27°, characteristic of a partially ordered layered polymer network with poor π–π stacking between the layers. The low-intensity diffraction arises from electrostatic repulsion between guanidinium cations, which disrupts long-range order, and promotes irregular stacking (Figure 2b). This behavior is consistent with previously reported guanidinium-based COPs [32].

Fourier transform infrared (FT-IR) spectroscopy verified successful imine bond formation in DhaTG(Cl^-), showing disappearance of the C═O stretch (1672 cm^{-1}), and N–H stretches (3321 and 3206 cm^{-1}), coupled with the emergence of a C═N bond (1622 cm^{-1}) (Figure 2c). Solid-state ^{13}C NMR spectroscopy confirmed the characteristic C═N resonance at approximately 149 ppm (Figure S1). The Brunauer-Emmett-Teller (BET) surface areas determined from N_2 (77 K) and CO_2 (195 K) adsorption isotherms were 69.9 and 54.9 m^2 g^{-1}, respectively (Figure 2d and Figure S2). The relatively low surface area may stem from strong interlayer electrostatic repulsion, intrinsic low structural order, and spontaneous self-exfoliation into ultrathin nanosheets [33, 34]. N_2 adsorption further confirmed a dominant pore size of 1.4 nm, which is in good agreement with the simulated result obtained via Zeo++ (Figure S3). Scanning and transmission electron microscopy (SEM/TEM) confirmed a lamellar morphology (Figure 2e,f; Figures S4 and S5), resulting from strong interlayer electrostatic repulsion. This repulsion weakens π–π stacking, promotes self-exfoliation, and facilitates IO_3^- transport. Moreover, DhaTG(Cl^-) retained its structural integrity upon exposure to various organic solvents and 100 kGy doses of γ irradiation, as confirmed by PXRD (Figure 2g).

2.2 | Adsorption Performance of DhaTG(Cl^-)

Batch adsorption isotherms were measured by equilibrating DhaTG(Cl^-) (2 g L^{-1}) with IO_3^- solutions of varying initial concentrations. Residual IO_3^- was quantified spectrophotometrically after reduction to I_3^-. The data fitted the Langmuir model well, yielding a high anion exchange-reduction capacity of 1093.7 mg g^{-1} (Figure 3a; Figures S6 and S7 and Tables S1 and S2), surpassing most reported materials (Figure 3b and Table S3).

Adsorption kinetics were remarkably rapid. Specifically, adding 5 mg DhaTG(Cl^-) to 2.5 mL of 50 ppm IO_3^- solution achieved >90% removal within 10 min, >95% within 30 min, and >99% within 1 h (Figure 3c). The kinetics followed a pseudo-second-order model ($R^2 > 0.9999$, Tables S4 and S5). The high distribution coefficient ($K_d = 2.17 \times 10^5$ mL g^{-1}) further confirmed strong affinity and rapid uptake (Figure S8 and Tables S6 and S7).

16163028, 2026, 75, Downloaded from https://advanced.onlinelibrary.wiley.com/doi/10.1002/adfm.77703 by Shengjian Ma - University Of North Texas Willis Library , Wiley Online Library on [21/10/2026]. See the Terms and Conditions (https://onlinelibrary.wiley.com/terms-and-conditions) on Wiley Online Library for rules of use; OA articles are governed by the applicable Creative Commons License

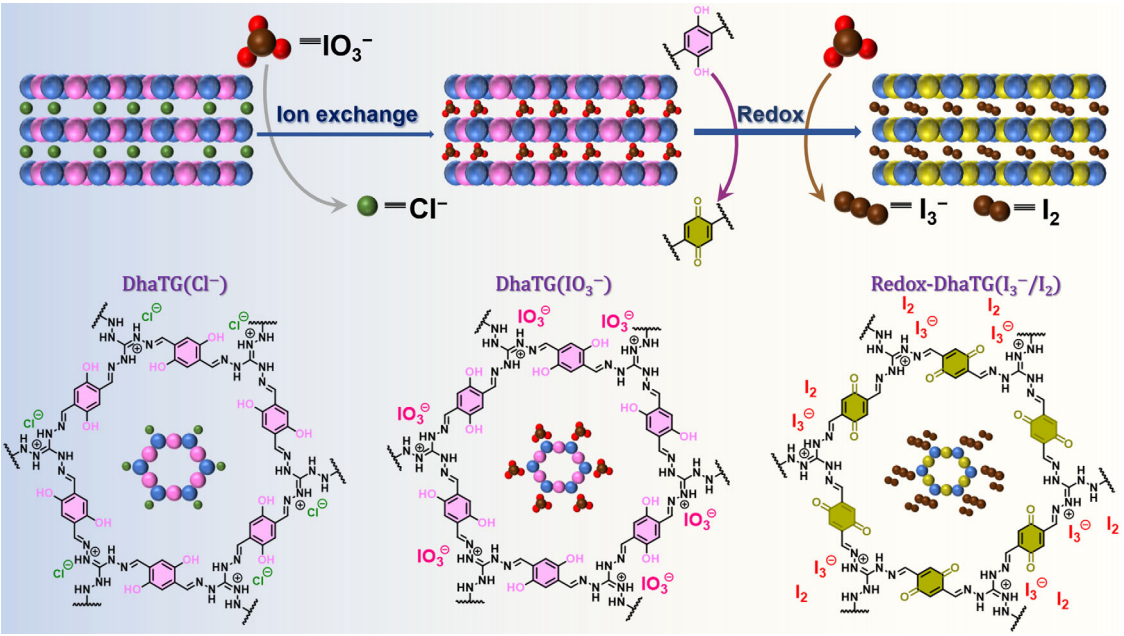


FIGURE 1 | Schematic representation of ion exchange–redox mechanisms for efficient IO_3^- removal.

This exceptional performance is attributed to the layered structure of DhaTG(Cl^-), providing abundant accessible sites, enabling synergistic electrostatic interaction and redox activity.

Since pH control is essential in real-world nuclear wastewater treatment, we evaluated the influence of pH on IO_3^- adsorption by DhaTG(Cl^-). Batch experiments were conducted using a solid–liquid ratio of 2 g L^{-1} and 25 ppm IO_3^- solutions at various pH levels. As shown in Figure 4a, DhaTG(Cl^-) maintained >99% IO_3^- removal efficiency over a wide pH range of 1–9. However, efficiency dropped sharply to 4.3% at pH 11, due to guanidinium deprotonation, creating electrostatic repulsion against IO_3^-.

To assess selectivity, competitive adsorption experiments were performed in the presence of equimolar concentrations of common anions (SO_4^{2-}, Cl^-, CO_3^{2-}, and NO_3^-), along with 1 mM IO_3^-. Remarkably, IO_3^- removal remained above 99% in all cases (Figure 4b). Considering that SO_4^{2-} and NO_3^- are typically abundant in nuclear wastewater, we further investigated their influence by increasing their molar ratios relative to IO_3^- from 1:1 to 100:1. As a result, DhaTG(Cl^-) retained high removal efficiencies of 77.7% (in the presence of SO_4^{2-} competing ion) and 94.4% (in the presence of NO_3^- competing ion), respectively (Figure 4c,d; Table S8). Further quantification by ion chromatography (IC) under equimolar competing anion conditions confirmed preferential IO_3^- uptake, with capacities of 1.02, 0.25, and 0.20 mmol g^{-1} for IO_3^-, NO_3^-, and SO_4^{2-}, respectively (Figure S9 and Table S9).

Performance was validated in simulated Beishan and Hanford nuclear-contaminated groundwaters (Table S10 and S11) containing high concentrations of competing anions (1 ppm IO_3^-). Increasing adsorption time from 12 to 48 h at a solid–liquid ratio of 5 g L^{-1} significantly improved removal: from 39.6% to 86.8% (Beishan) and from 21.7% to 95.7% (Hanford) (Figure 4e,f; Table S12). These results further confirm the high selectivity and practical applicability of DhaTG(Cl^-) for IO_3^- capture in complex aqueous environments. Energy-dispersive X-ray spectroscopy (EDS) mapping confirmed uniform elemental distribution before and after adsorption and revealed IO_3^- replacing Cl^-, supporting ion exchange (Figure 4g,h).

2.3 | Mechanistic Insights Into IO_3^- Adsorption by DhaTG(Cl^-)

To investigate the adsorption mechanism of IO_3^- by DhaTG(Cl–), X-ray photoelectron spectroscopy (XPS) survey spectra were employed. As shown in Figure 5a, survey spectra showed complete Cl 2*p* loss and I 3*d* emergence after adsorption. High-resolution I 3*d* spectra revealed only trace IO_3^- peaks (635.00 and 623.50 eV); dominant peaks at 632.06/620.60 eV and 630.11/618.63 eV were assigned to I_2 and I_3^-, respectively (Figure 5b) [22]. These findings confirmed the on-site reduction of IO_3^- to lower-valence iodine species. Furthermore, O 1*s* spectra showed the original C–O peak (532.86 eV) and a new C═O peak (531.20 eV) post-adsorption (Figure 5c and Figure S10), directly evidencing electron transfer from phenolic hydroxyl groups to IO_3^- and skeleton oxidation. These results support a two-step synergistic mechanism: (1) ion exchange (IO_3^-/Cl^-), followed by (2) redox reaction where phenolic groups reduce IO_3^- to I_2/I_3^-, oxidizing to quinones (Figure 5d).

To further confirm the synergic effect of such adsorption, regenerability of DhaTG(Cl^-) was evaluated. Herein, a mild regenerative solution containing L-ascorbic acid, NaCl, and ethanol was employed (Figure S11). This formulation was designed to concurrently restore the redox-active phenolic sites (via reduction by ascorbic acid) and the ion-exchange capacity (via Cl^- vs I^-/I_3^- exchange), while ethanol facilitated the desorption of I_2. After three cycles, the adsorption capacity of IO_3^- remained 808.5 mg g^{-1} (Figure 5e; Table S12). The PXRD pattern of DhaTG(Cl^-) after three cycles exhibits the same characteristic broad peaks (Figure S12a), demonstrating that the poorly ordered layered stacking

16163028, 2026, 75, Downloaded from https://advanced.onlinelibrary.wiley.com/doi/10.1002/adfm.77703 by Shengjian Ma - University Of North Texas Willis Library , Wiley Online Library on [21/10/2026]. See the Terms and Conditions (https://onlinelibrary.wiley.com/terms-and-conditions) on Wiley Online Library for rules of use; OA articles are governed by the applicable Creative Commons License

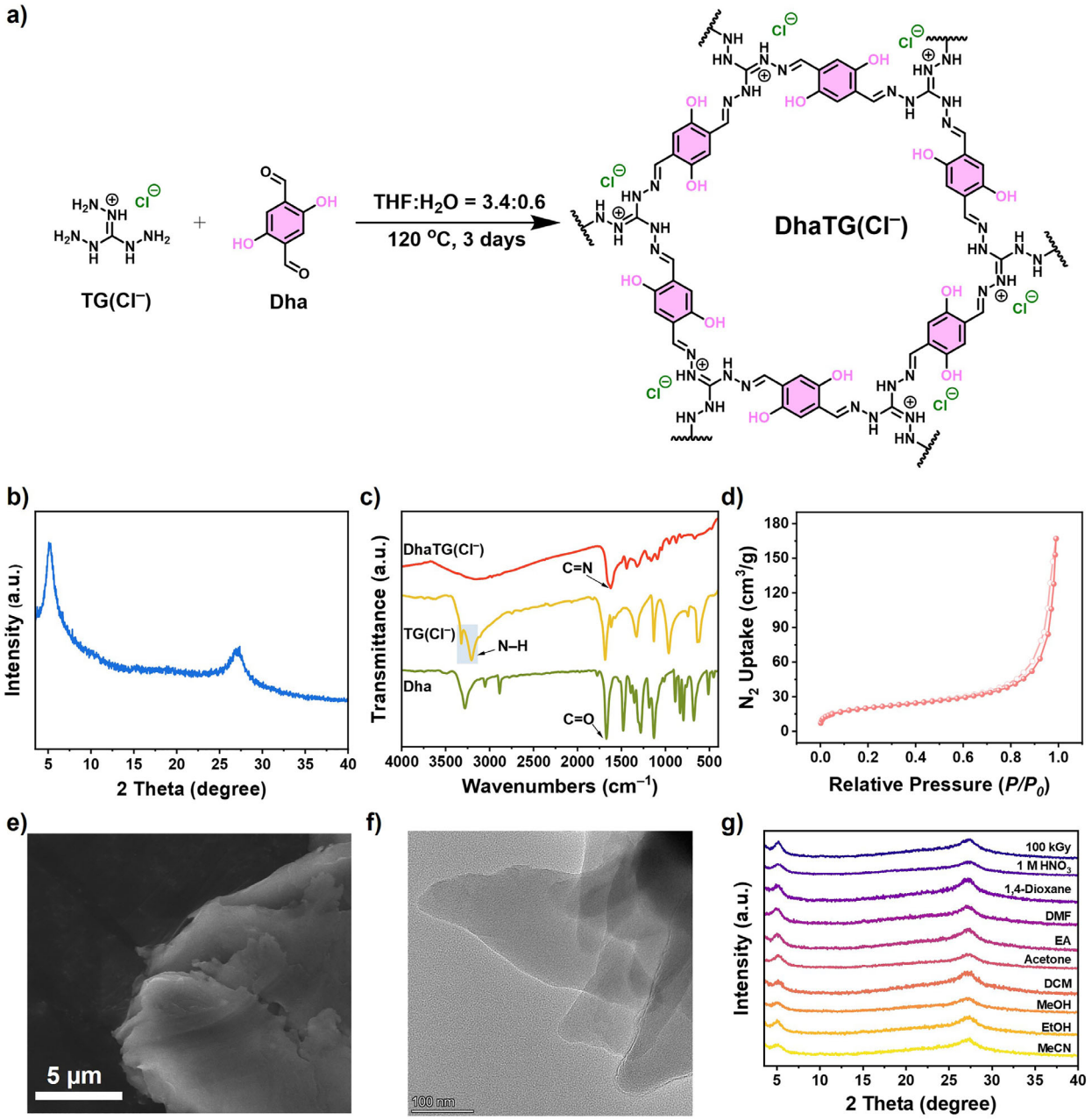


FIGURE 2 | Characterization of DhaTG(Cl⁻). (a) Synthesis route of DhaTG(Cl⁻). (b) PXRD pattern. (c) FT-IR spectra. (d) N_2 sorption isotherm. (e) SEM image and (f) TEM image of DhaTG(Cl⁻). (g) PXRD patterns of DhaTG(Cl⁻) after exposure to different media and γ-ray irradiation.

is preserved. Further evidence from FT-IR and BET analyses (Figure S12b,c) reveals unchanged chemical functionality and porosity, while SEM images show no discernible morphological deterioration before and after the third regeneration cycle (Figure S12d–f). Though DhaTG(Cl⁻) shows the second-highest adsorption capacity for IO_3^-, it represents the first demonstration of reliable regenerability in a COP-based adsorbent for such a system [24], highlighting DhaTG(Cl⁻) as a cost-effective and high-performance adsorbent.

Visual and spectral changes provided further confirmation of the redox mechanism. The color of DhaTG(Cl⁻) darkened visibly after exposure to IO_3^- solution (Figure S13), consistent with the formation of lower-valence iodine species such as I_2. Additionally, minimal iodine leaching (≤2.55% after 12 h) was observed under all tested conditions (pH = 3 or, and 60°C), demonstrating effective retention within the iCOP (Figure S14 and Table S13). FT-IR spectra of the post-adsorption material showed no IO_3^- peak (ca. 760 cm^{-1}) but revealed newly formed C═O bonds at 1645 cm^{-1}, corresponding to the oxidation of phenolic hydroxyl groups to quinone moieties in redox-DhaTG(I) (Figure S15). To address the concern that HNO_3 might act as an interfering oxidant, the material was immersed in 1 M HNO_3 for 24 h. FT-IR analysis showed that while NO_3^- was adsorbed, the phenolic hydroxyl groups remained intact without oxidative degradation (Figure S16).

16163028, 2026, 75, Downloaded from https://advanced.onlinelibrary.wiley.com/doi/10.1002/adfm.77703 by Shengqian Ma - University Of North Texas Willis Library , Wiley Online Library on [21/10/2026]. See the Terms and Conditions (https://onlinelibrary.wiley.com/terms-and-conditions) on Wiley Online Library for rules of use; OA articles are governed by the applicable Creative Commons License

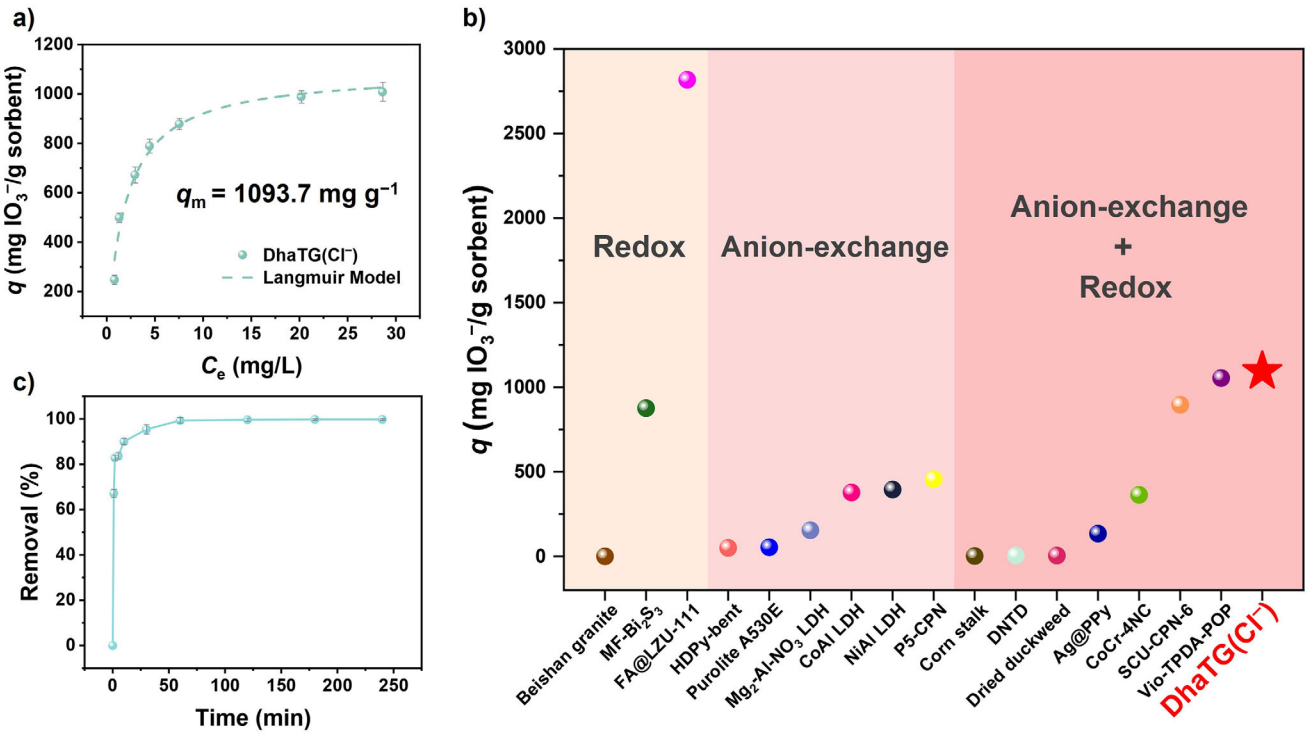


FIGURE 3 | Sorption performances of DhaTG(Cl^-). (a) Adsorption isotherms curves and (c) adsorption kinetics curve of DhaTG(Cl^-) to IO_3^-. (b) Comparison of adsorption capacities of various materials.

2.4 | Functional Group Synergy in iCOPs

To deconvolute the roles of ion exchange and redox sites, we designed a series of structurally related iCOPs by systematically varying the proportions of cationic guanidinium sites (for ion exchange) and phenolic hydroxyl groups (for redox activity), to deconvolute their individual and synergistic roles (Figure S17). Replacing the –OH groups of Dha with $-OCH_3$ yielded a iCOP with only guanidinium sites, DMTATG(Cl^-), which only shows 75.4 mg g^{-1} IO_3^- adsorption capacity (Figure 6a and Figure S18a). O 1*s* spectra of DMTATG(Cl^-) showed no C—O to C═O transformation post-adsorption, confirming absent redox activity (Figure S19). These results clearly demonstrated that ion exchange contributes to uptake but is insufficient for high efficiency. Conversely, replacing cationic TG with neutral tris(4-aminophenyl)benzene (TAPB) yielded a COP with only phenolic groups, TAPBD. Its IO_3^- uptake was negligible (1.8 mg g^{-1}) (Figure 6b; Figure S18b), indicating redox alone is ineffective without electrostatic attraction. These results highlight the essential synergy between both functionalities.

To further explore the impact of redox functionality, we synthesized two additional iCOPs by co-polymerizing redox-active Dha (D) with redox-inert 1,4-phthalaldehyde (TPA, T) in controlled molar ratios of D:T = 7:3 and 3:7, yielding $D_7T_3TG(Cl^-)$ and $D_3T_7TG(Cl^-)$, respectively (Figure 6c). Adsorption capacities decreased with lower redox content, from 581.8 mg g^{-1} for $D_7T_3TG(Cl^-)$ to 334.3 mg g^{-1} for $D_3T_7TG(Cl^-)$ (Figure S20). In comparison, the fully functionalized DhaTG(Cl^-) achieved a notably high capacity (1093.7 mg g^{-1}), confirming that redox activity primarily drives capacity, while the cationic network enables efficient anion access and uptake.

2.5 | DFT-Modelling of IO_3^- Ion Exchange–Redox Molecular Mechanisms

To elucidate the molecular basis for the unprecedented performance of DhaTG(Cl^-), we performed density functional theory (DFT) calculations at the GGA PBE level, employing a full electronic scalar-relativistic TZ basis (computational details in Supporting Information). A representative fragment of the iCOP, receptor 1 (Figure 7a; Figure S21), was modeled by terminating C═N breakpoints with methyl groups. This fragment incorporates three hydroquinone moieties capable of supplying the six electrons required for the complete reduction of IO_3^- to I^-, enabling simulation within an isolated gas-phase system [$(1^+)(IO_3^-)$].

2.5.1 | Initial Binding and Activation

IO_3^- binds exothermically to receptor 1 forming complex 2 (ΔG = –352.3 kJ mol^{-1}, Figure 7b; Figure S22), significantly exceeding its hydration energy (–326 kJ mol^{-1}). This strong binding arises not only from Coulombic attraction but also from the formation of two specific hydrogen bonds: O–H(hydroquinone)•••OIO_2 and N–H(guanidinium)•••OIO_2. It is consistent with the observed high efficiency and high rate of its binding by the DhaTG(Cl^-) sorbent. Quantum Theory of Atoms in Molecules (QTAIM)

16163028, 2026, 75, Downloaded from https://advanced.onlinelibrary.wiley.com/doi/10.1002/adfm.77703 by Shengqian Ma - University Of North Texas Willis Library , Wiley Online Library on [21/10/2026]. See the Terms and Conditions (https://onlinelibrary.wiley.com/terms-and-conditions) on Wiley Online Library for rules of use; OA articles are governed by the applicable Creative Commons License

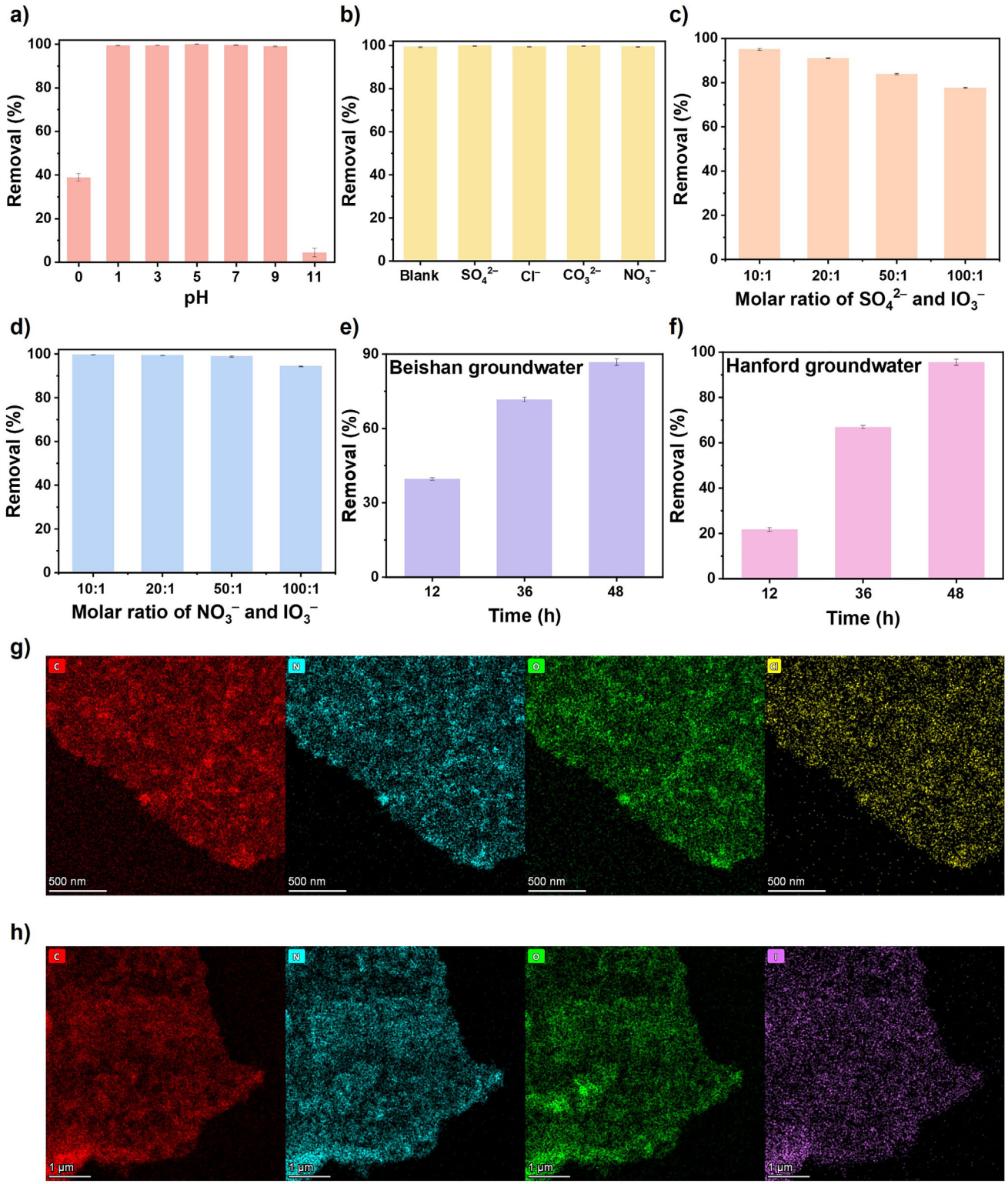


FIGURE 4 | IO_3^- scavenging studies on DhaTG(Cl^-). Removal of IO_3^- by DhaTG(Cl^-) under (a) different pH values and (b) typical competitive ions. Effects of excess (c) SO_4^{2-} and (d) NO_3^- on the adsorption of IO_3^-. Removal of IO_3^- by DhaTG(Cl^-) from simulated nuclear-contaminated (e) Beishan and (f) Hanford groundwaters. EDS mapping images of DhaTG(Cl^-) (g) before and (h) after adsorption of IO_3^-.

analysis confirmed these interactions (Figure S23). Crucially, during coordination the anion IO_3^- accepted the proton of the N—H bond of the receptor and was bound to it as a molecule of iodic acid. This initial proton transfer is critical for subsequent reduction steps.

2.5.2 | Stepwise Proton-Coupled Electron Transfer (PCET) Reduction Pathway

The lowest-energy reduction pathway proceeds via sequential PCET events from the hydroquinone donors to the coordinated

16163028, 2026, 75, Downloaded from https://advanced.onlinelibrary.wiley.com/doi/10.1002/adfm.77703 by Shengqian Ma - University Of North Texas Willis Library , Wiley Online Library on [21/10/2026]. See the Terms and Conditions (https://onlinelibrary.wiley.com/terms-and-conditions) on Wiley Online Library for rules of use; OA articles are governed by the applicable Creative Commons License

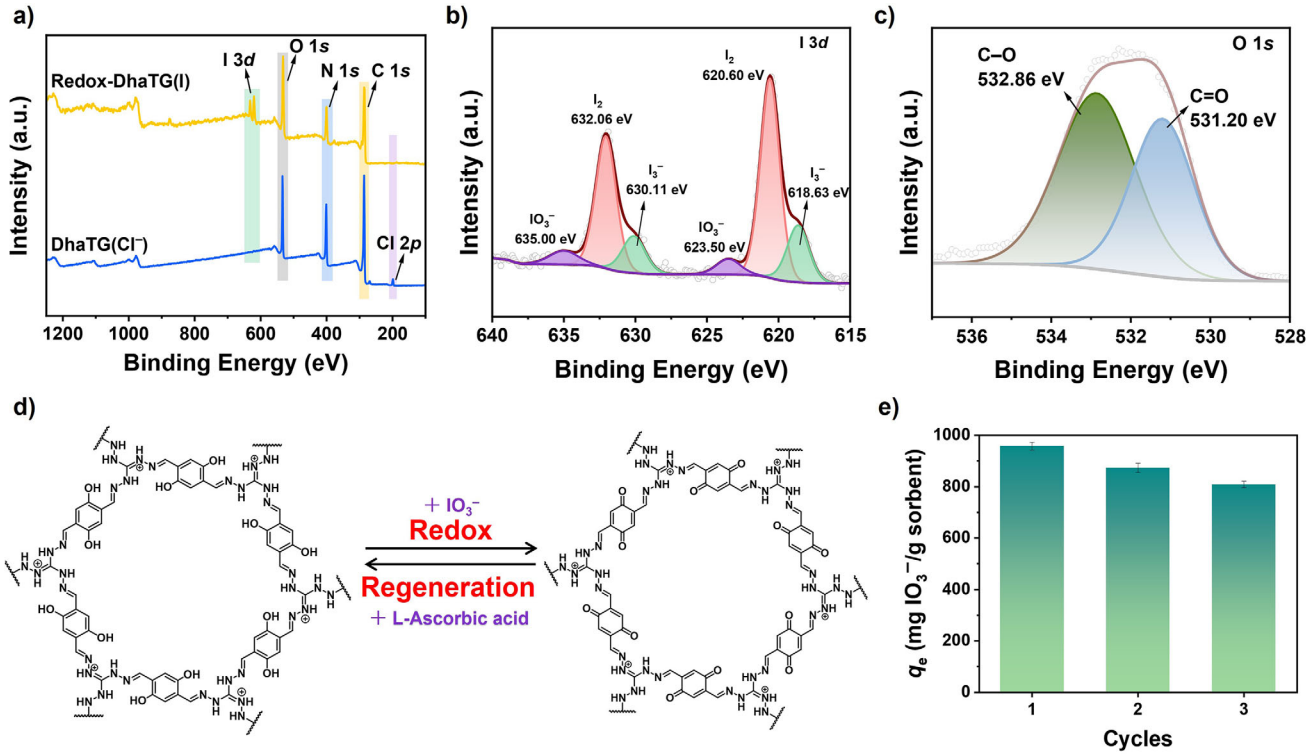


FIGURE 5 | Adsorption mechanism investigation. (a) XPS survey spectra of DhaTG(Cl^-) before and after adsorption of IO_3^-. (b) I 3*d* XPS spectra of DhaTG(Cl^-) after adsorption of IO_3^-. (c) O 1*s* XPS spectra of DhaTG(Cl^-) after adsorption of IO_3^-. (d) Schematic view of the process of redox and regeneration reactions. (e) Comparison of uptake capacities of IO_3^- in three cycles.

HIO_3 substrate. i) I(V) → I(III) reduction. The reduction initiates with PCET from the hydroquinone group directly involved in H-bonding to an oxygen atom of IO_3^-.This concerted transfer yields complex 3 (Figure 7c; Figure S24), characterized as an I(III) species. Thus, the reduction of I(V)→I(III) occurs with a large energy gain in one act. In 3, the *ortho*-iodic acid molecule [$I(OH)_3$] is linked to 1 via a strong, short C═O•••H–O–I hydrogen bond (1.779 Å) and weaker N–H•••O–I (2.230 Å) and C–H•••O–I (2.24 Å) interactions (QTAIM confirmed, Figure S25). ii) Further reduction and O–I bond cleavage. A subsequent PCET event from a remote hydroquinone group to the I(III) center in complex 3 forms complex 4 (Figure 7d; Figure S26). Cleavage of an O–I bond and water elimination from complex 4 yields complex 5 (Figure 7e; Figures S27 and S28), featuring an unusual I(II) species. QTAIM analysis revealed this intermediate is stabilized by coordination bonds resembling hypervalent interactions: two N→I bonds (characteristic of halogen bonding) and one O→I bond [35, 36]. The I(II) oxidation state in 5 is unstable, prompting immediate electron transfer from the same hydroquinone donor, reducing I(II) to I(I) and forming complex 6 (Figure 7f and Figure S29), where iodine retains coordination via a hydrogen bond to the eliminated water molecule. iii) Final Reduction to I^-. The ultimate PCET step involves reduction of I(I)→I(0) with the transfer of a proton and an electron from the second remote hydroquinone to the (I–OH) fragment in 6, generating another water molecule and resulting in complex 7 (Figure 7g; Figure S30). A lengthened N→I halogen bond exists in 7 compared to that in 6. The final stage of the reduction I^0→I^- occurs in 7 with a large gain in energy, yielding system 8 (Figure 7h). In 8, the I^- anion remains coordinated to the oxidized receptor via Coulombic forces and an I^-•••H–N hydrogen bond.

Thus, the DFT modeling reveals a critical stepwise PCET mechanism. In the isolated system [($DhaTG^+$)(IO_3^-)], the reduction of the IO_3^- anion can easily proceed along the path of the lowest energy stepwise. These calculations explicitly show how the guanidinium group (ion exchange, initial protonation) and hydroquinone groups (redox donors) act cooperatively within the rigid network to facilitate efficient IO_3^- capture and reduction.

3 | Conclusion

This work demonstrates an effective strategy for radionuclide remediation through the rational design of DhaTG(Cl^-), a dual-functional iCOP that synergizes ion exchange and redox activity to achieve superior iodate (IO_3^-) capture. By integrating cationic guanidinium sites and redox-active phenolic groups within a single covalent skeleton, we unlock a cooperative mechanism: rapid electrostatic uptake of IO_3^- followed by on-site reduction to I_2/I_3^-. This results in a remarkable combination of high capacity (1093.7 mg g^{-1}) and fast kinetics (99% removal in 1 h), mild regeneration (retaining 74% capacity after 3 cycles), exceptional affinity (K_d = 2.17 × 10^5 mL g^{-1}), and unprecedent regenerability under mild treatment. DFT calculations evidently demonstrate that this ion exchange-redox pathway proceeds via stepwise PCET mechanism.

16163028, 2026, 75, Downloaded from https://advanced.onlinelibrary.wiley.com/doi/10.1002/adfm.77703 by Shengqian Ma - University Of North Texas Willis Library , Wiley Online Library on [21/10/2026]. See the Terms and Conditions (https://onlinelibrary.wiley.com/terms-and-conditions) on Wiley Online Library for rules of use; OA articles are governed by the applicable Creative Commons License

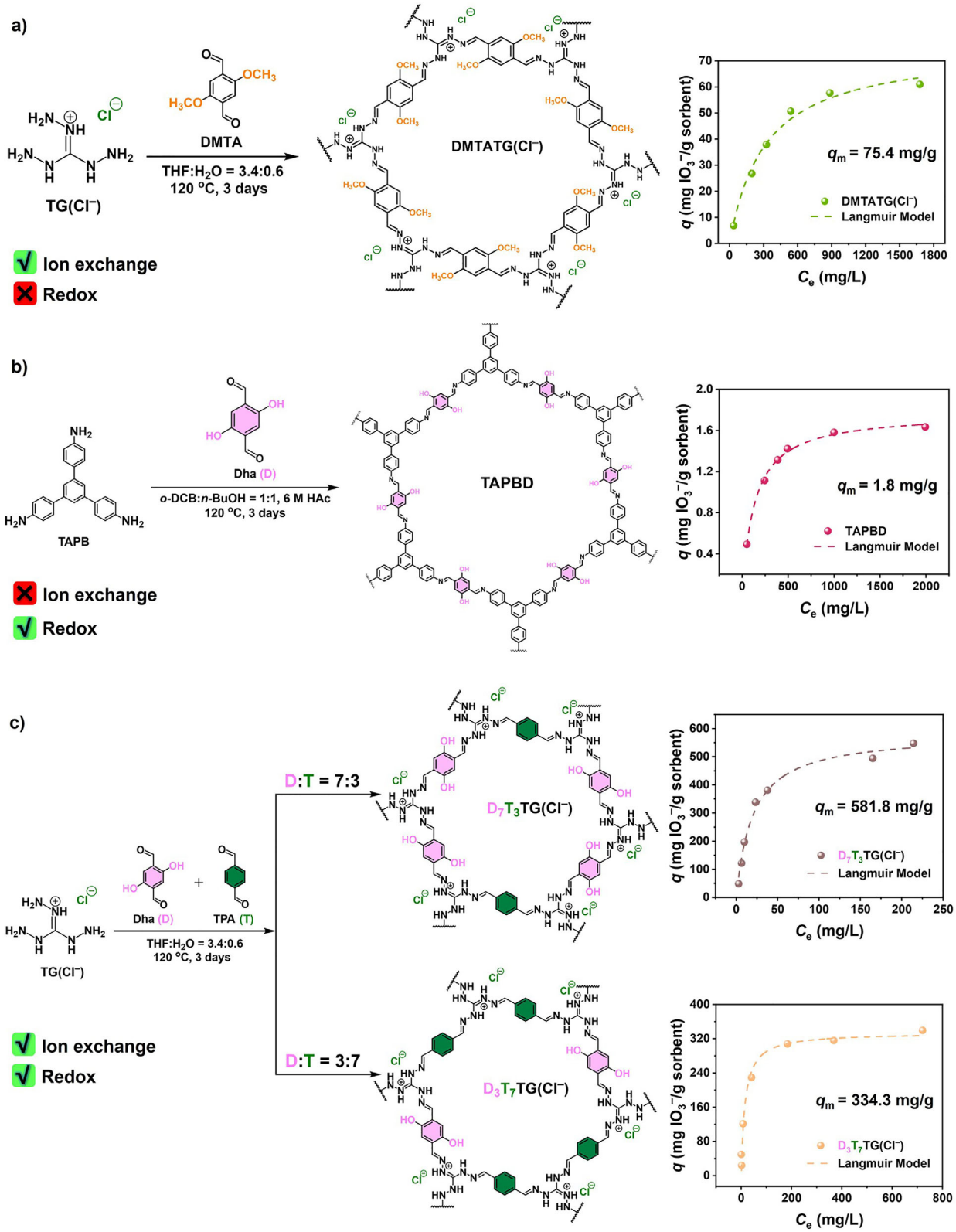


FIGURE 6 | Functional site regulation of COPs. Reactions and IO_3^- isotherms curves of (a) DMTATG(Cl^-), (b) TAPBD, (c) $D_7T_3TG(Cl^-)$, and $D_3T_7TG(Cl^-)$.

16163028, 2026, 75, Downloaded from https://advanced.onlinelibrary.wiley.com/doi/10.1002/adfm.77703 by Shengjian Ma - University Of North Texas Willis Library , Wiley Online Library on [21/10/2026]. See the Terms and Conditions (https://onlinelibrary.wiley.com/terms-and-conditions) on Wiley Online Library for rules of use; OA articles are governed by the applicable Creative Commons License

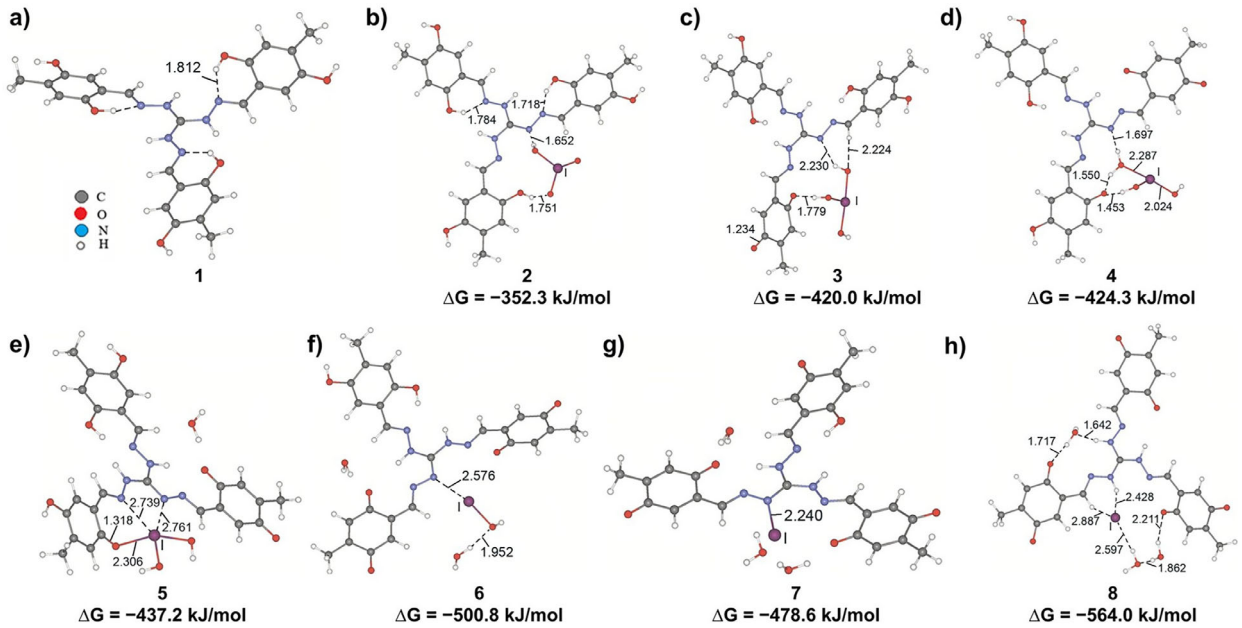


FIGURE 7 | Computational simulations of IO_3^- sorption by DhaTG(Cl^-). Structures of receptor 1 (a), as well as complexes 2 (b), 3 (c), 4 (d), 5 (e), 6 (f), 7 (g), and 8 (h). The formation energy of each complex is also shown. Bond lengths are given in Å.

This work establishes a powerful design principle for multifunctional iCOPs, combining targeted ion exchange with redox pathways for efficient capture of specific radionuclides. Our findings open new avenues for next-generation adsorbents addressing critical challenges in environmental remediation and nuclear waste management.

Acknowledgements

We acknowledge the financial support of the National Nature Science Foundation of China (22171210). Partial support from the Robert A. Welch Foundation (B-0027) (S.M.) and the Ongoing Research Funding Program (ORF-2026-79), King Saud University, Riyadh, Saudi Arabia (AN) is also acknowledged.

Conflicts of Interest

The authors declare no conflicts of interest.

Data Availability Statement

The data supporting the findings of this study are available from the corresponding author upon reasonable request.

References

1. International Energy Agency, *Electricity 2024*, (International Energy Agency, 2024).

2. S. Saha, S. Roy, P. Mathi, and J. A. Mondal, "Adsorption of Iodine Species (I_3–, I^-, and IO_3–) at the Nuclear Paint Monolayer–Water Interface and Its Relevance to a Nuclear Accident Scenario," *The Journal of Physical Chemistry A* 124 (2020): 6726–6734, https://doi.org/10.1021/acs.jpca.0c04893.

3. H. M. Wainwright, K. Whiteaker, H. Gonzalez-Raymat, et al., "The Iodine-129 Paradox in Nuclear Waste Management Strategies," *Nature Sustainability* 8 (2025): 1391–1399, https://doi.org/10.1038/s41893-025-01629-2.

4. C. Fernández Martín, J. C. Alonso Farto, I. Gómez Fernández, et al., "Genotoxic Effects of Ablative Treatment With I-131 Determined Through the Analysis of Dicentric Chromosomes in Peripheral Blood Lymphocytes. Can it Influence the Clinical Management of Patients With Differentiated Thyroid Carcinoma?," *Radiation Physics and Chemistry* 223 (2024): 111927, https://doi.org/10.1016/j.radphyschem.2024.111927.

5. N. Yoshida and J. Kanda, "Tracking the Fukushima Radionuclides," *Science* 336 (2012): 1115–1116, https://doi.org/10.1126/science.1219493.

6. J. A. Kenyon, K. O. Buesseler, N. Casacuberta, et al., "Distribution and Evolution of Fukushima Dai-ichi derived ^{137}Cs, ^{90}Sr, and ^{129}I in Surface Seawater off the Coast of Japan," *Environmental Science & Technology* 54 (2020): 15066–15075, https://doi.org/10.1021/acs.est.0c05321.

7. S. Zhang, C. Xu, D. Creeley, et al., "Iodine-129 and Iodine-127 Speciation in Groundwater at the Hanford Site, U.S.: Iodate Incorporation Into Calcite," *Environmental Science & Technology* 47 (2013): 9635–9642, https://doi.org/10.1021/es401816e.

8. X. Zhang, J. Maddock, T. M. Nenoff, M. A. Denecke, S. Yang, and M. Schröder, "Adsorption of Iodine in Metal–Organic Framework Materials," *Chemical Society Reviews* 51 (2022): 3243–3262, https://doi.org/10.1039/D0CS01192D.

9. X. Li, Z. Jia, J. Zhang, et al., "Moderate and Universal Synthesis of Undoped Covalent Organic Framework Aerogels for Enhanced Iodine Uptake," *Chemistry of Materials* 34 (2022): 11062–11071, https://doi.org/10.1021/acs.chemmater.2c03117.

10. Y. Xie, Q. Rong, F. Mao, et al., "Engineering the Pore Environment of Antiparallel Stacked Covalent Organic Frameworks for Capture of Iodine Pollutants," *Nature Communications* 15 (2024): 2671, https://doi.org/10.1038/s41467-024-46942-0.

11. H.-R. Li, S. Wu, X. Jing, et al., "Polymer-on-HOF: A New Strategy for Fabricating "Armour-Plated" HOFs to Sequester Radioactive Anions," *Science China Chemistry* 67 (2024): 2958–2967, https://doi.org/10.1007/s11426-024-2024-8.

12. X. Guo, Y. Li, M. Zhang, et al., "Colyliform Crystalline 2D Covalent Organic Frameworks (COFs) With Quasi-3D Topologies for Rapid I_2

16163028, 2026, 75, Downloaded from https://advanced.onlinelibrary.wiley.com/doi/10.1002/adfm.77703 by Shengjian Ma - University Of North Texas Willis Library , Wiley Online Library on [21/10/2026]. See the Terms and Conditions (https://onlinelibrary.wiley.com/terms-and-conditions) on Wiley Online Library for rules of use; OA articles are governed by the applicable Creative Commons License

Adsorption," *Angewandte Chemie International Edition* 59 (2020): 22697–22705, https://doi.org/10.1002/anie.202010829.

13. Q. Li, W. Guo, Z. Wang, L. L. Tan, and L. Shang, "Tailoring Electron-Rich Fluorescent Supramolecular Organic Frameworks for Efficient Capture and Visual Monitoring of Iodine," *Advanced Functional Materials* 35 (2025): 2413694, https://doi.org/10.1002/adfm.202413694.

14. A. Al-Mamoori, M. Alsalbokh, S. Lawson, A. A. Rownaghi, and F. Rezaei, "Development of Bismuth-Mordenite Adsorbents for Iodine Capture From Off-Gas Streams," *Chemical Engineering Journal* 391 (2020): 123583, https://doi.org/10.1016/j.cej.2019.123583.

15. C. Yan, J. Li, C. Tan, et al., "Cuprous Oxide-Based Cationic Hydrogel by the Integration of Enrichment and Immobilization of Radioiodine (I^-, IO_3^-) in Aqueous Solution," *ACS Applied Materials & Interfaces* 15 (2023): 28135–28148, https://doi.org/10.1021/acsami.3c04816.

16. B. Tai, B. Li, L. He, et al., "Flexible Interdigitated Layered Framework With Multiple Accessible Active Sites for High-Performance CH_3I Capture," *Science China Chemistry* 67 (2024): 1569–1577, https://doi.org/10.1007/s11426-023-1860-5.

17. S. Deng, X. Kong, X. Fu, et al., "Cage-Based Metal–Organic Framework Featuring a Double-Yolk Core–Shell $U_6L_3@U_{18}L_{14}$ Structure for Iodine Capture," *Inorganic Chemistry* 64 (2025): 224–231, https://doi.org/10.1021/acs.inorgchem.4c04490.

18. J. S. Hoskins, T. Karanfil, and S. M. Serkiz, "Removal and Sequestration of Iodide Using Silver-Impregnated Activated Carbon," *Environmental Science & Technology* 36 (2002): 784–789, https://doi.org/10.1021/es010972m.

19. X. Liu, M. Xiao, P. Chen, et al., "In-Situ Synthesis of Layered Double Hydroxides With Tunable Basal Spacing for Efficient Iodide Over Iodate Adsorption Selectivity," *Science China Chemistry* 68 (2025): 2424–2432, https://doi.org/10.1007/s11426-024-2391-0.

20. Q. Zhao, R. Liu, Z. Wang, G. Chen, T. Duan, and L. Zhu, "Core-Shell Ag@polypyrrole for Synchronous Pre-Enrichment and Immobilization of Iodine (I^-, IO_3^-) From Liquid Radioactive Waste," *Environmental Science: Nano* 11 (2024): 149.

21. N. A. Wall, E. Maulden, E. J. Gager, et al., "Functionalized Clays for Radionuclide Sequestration: A Review," *ACS Earth and Space Chemistry* 6 (2022): 2552.

22. C. Yan, B. Zhang, Y. Liu, and Z. He, "Introducing Micro Flowerlike Bismuth Sulfide for Iodate Anion Removal," *Inorganic Chemistry* 64 (2025): 7698–7705, https://doi.org/10.1021/acs.inorgchem.5c00732.

23. Y. Lin, C. Wang, X. Zhao, et al., "Imaging the Encapsulation of Formic Acids in Single LZU-111 COFs as Reductants, Microreactors, and Optical Microcavities for Record-High Iodate Anion Removal," *The Journal of Physical Chemistry Letters* 16 (2025): 9135–9142, https://doi.org/10.1021/acs.jpclett.5c02174.

24. Y. Guo, C. Ni, Y. Lei, et al., "Enhanced Pd(II) Capture and Recycling Through Synergistic N–O Coordination in Crown Ether-Based Covalent Organic Polymers," *Chemical Engineering Journal* 528 (2026): 172689, https://doi.org/10.1016/j.cej.2026.172689.

25. H. Ali, Y. Orooji, A. Y. A. Alzahrani, et al., "Innovative Morphological Modifications of Porous Organic Polymers for Advanced Photocatalytic Applications," *Coordination Chemistry Reviews* 543 (2025): 216884, https://doi.org/10.1016/j.ccr.2025.216884.

26. C. Yang, K. Wang, W. Lyu, et al., "Nanofibrous Porous Organic Polymers and Their Derivatives: From Synthesis to Applications," *Advanced Science* 11 (2024): 2400626, https://doi.org/10.1002/advs.202400626.

27. A. Alam, A. Hassan, and N. Das, "Triptycene-Based Porous Organic Network Polymers: From Synthesis to Applications," *Progress in Materials Science* 155 (2026): 101528, https://doi.org/10.1016/j.pmatsci.2025.101528.

28. C. Gao, J. Li, S. Yin, J. Sun, and C. Wang, "Redox-Triggered Switching in Three-Dimensional Covalent Organic Frameworks," *Nature Communications* 11 (2020): 4919, https://doi.org/10.1038/s41467-020-18588-1.

29. D. Chen, Z. Ren, M. Shi, F. Zhou, and R. Zhao, "Molecular Regulation of Viologen-Based Porous Organic Polymers for Electrochemical Iodate Removal," *Advanced Functional Materials* 36 (2025): 25942, https://doi.org/10.1002/adfm.202525942.

30. L. Antipova, O. Tripachev, A. Rybakova, et al., "Autocatalyzed Kinetics of 6-Electron Electroreduction of Iodic Acid Studied by Rotating Disk Electrode Technique," *Catalysts* 14 (2024): 437, https://doi.org/10.3390/catal14070437.

31. J. E. Nutting, J. B. Gerken, A. G. Stamoulis, D. L. Bruns, and S. S. Stahl, ""How Should I Think About Voltage? What Is Overpotential?": Establishing an Organic Chemistry Intuition for Electrochemistry," *The Journal of Organic Chemistry* 86 (2021): 15875–15885, https://doi.org/10.1021/acs.joc.1c01520.

32. H.-J. Da, C.-X. Yang, and X.-P. Yan, "Cationic Covalent Organic Nanosheets for Rapid and Selective Capture of Perrhenate: An Analogue of Radioactive Pertechnetate From Aqueous Solution," *Environmental Science & Technology* 53 (2019): 5212–5220, https://doi.org/10.1021/acs.est.8b06244.

33. H.-M. Guo, X.-Y. Dong, S. Wang, Q.-Y. Wang, and S.-Q. Zang, "Constructing Energetic Covalent Organic Frameworks With High Stability and Low Sensitivity," *Chinese Chemical Letters* 35 (2024): 108537, https://doi.org/10.1016/j.cclet.2023.108537.

34. N. Zhang, X. Li, P. Li, and S. Tang, "Guanidinium Cationic Covalent Organic Nanosheets-Based Anion Exchange Composite Membrane for Fuel Cells," *International Journal of Hydrogen Energy* 48 (2023): 25972–25983, https://doi.org/10.1016/j.ijhydene.2023.03.332.

35. S. Yu, J. S. Ward, K.-N. Truong, and K. Rissanen, "Carbonyl Hypoiodites as Extremely Strong Halogen Bond Donors," *Angewandte Chemie International Edition* 60 (2021): 20739–20743, https://doi.org/10.1002/anie.202108126.

36. I.-R. Jeon, O. Jeannin, A. Robert, F. Barrière, and M. Fourmigué, "N -Iodophthalimide as a Halogen Bond Donor, A Comparison With N -Iodosuccinimide and N -Iodosaccharin," *CrystEngComm* 26 (2024): 6075–6081, https://doi.org/10.1039/D4CE00654B.

Supporting Information

Additional supporting information can be found online in the Supporting Information section.

Supporting File: adfm77703-sup-0001-SuppMat.docx.

16163028, 2026, 75, Downloaded from https://advanced.onlinelibrary.wiley.com/doi/10.1002/adfm.77703 by Shengjian Ma - University Of North Texas Willis Library , Wiley Online Library on [21/10/2026]. See the Terms and Conditions (https://onlinelibrary.wiley.com/terms-and-conditions) on Wiley Online Library for rules of use; OA articles are governed by the applicable Creative Commons License